PROCEEDINGS A

royalsocietypublishing.org/journal/rspa

Research

Cite this article: Bárcenas-Luque AJ, Blyth MG. 2026 The Moffatt–Pukhnachev flow: a new twist on an old problem. *Proc. R. Soc. A* **482**: 20250748.
https://doi.org/10.1098/rspa.2025.0748

Received: 28 August 2025
Accepted: 21 November 2025

Subject Areas:
applied mathematics, fluid mechanics

Keywords:
viscous fluid mechanics, thin films, multiple-scales analysis, coating flow

Author for correspondence:
M. G. Blyth
e-mail: m.blyth@uea.ac.uk

The Moffatt–Pukhnachev flow: a new twist on an old problem

A. J. Bárcenas-Luque[1] and M. G. Blyth[2]

[1]Department of Mechanics of Structures and Hydraulic Engineering, University of Granada, Granada 18001, Spain
[2]School of Mathematics, University of East Anglia, Norwich NR4 7TJ, UK

AJB-L , 0000-0001-6407-7697

The flow of a thin viscous film on the outside of a horizontal circular cylinder, whose angular velocity is time-periodic with specified frequency and amplitude, is investigated. The constant angular velocity problem was originally studied by Moffatt (Moffatt 1977 *J. Mécanique* **16**, 651–673) and Pukhnachev (Pukhnachev 1977 *J. Appl. Mech. Tech. Phys.* **18**, 344–351). Surface tension is neglected. The evolution equation for the film thickness is solved numerically for a range of oscillation amplitudes and frequency. A blow-up map charted in amplitude–frequency space reveals highly intricate fractal-like structures exhibiting self-similarity. For a general initial condition, numerical computations indicate that the film surface reaches a slope singularity at a finite time and tends to overturn. The high-frequency and low-frequency limits are examined asymptotically using a multiple-scales approach. At high frequency, the analysis suggests that an appropriate choice of initial profile can substantially delay the overturning time, and even yield a time-periodic solution. In the low-frequency limit, it is possible to construct a quasi-periodic solution that does not overturn if the oscillation amplitude lies below a threshold value. Above this value, the solution tends inexorably toward blow-up. It is shown how solutions exhibiting either a single-shock or a double-shock may be constructed in common with the steadily rotating cylinder problem.

1. Introduction

Moffat [1] studied the dynamics of a thin viscous liquid film coating the outside of a horizontal circular cylinder

THE ROYAL SOCIETY PUBLISHING

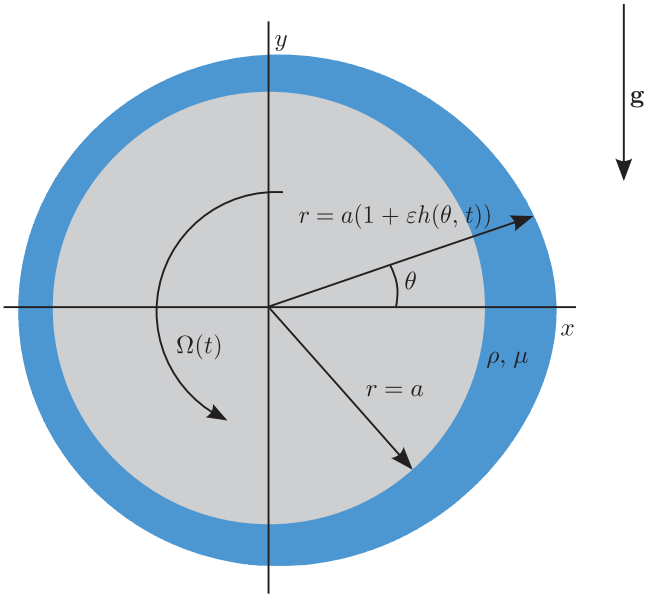

Figure 1. Sketch of the flow configuration: a thin viscous liquid film coats the outside of a circular cylinder of radius a, which is rotating with angular velocity $\Omega(t)$, where t is time. Gravity acts in the downward vertical direction as shown.

that is rotating about its axis at a constant rate. This problem has important practical applications ranging from industrial processes (Ribatski & Jacobi [2]) to applications in the art world (Herczynski *et al.* [3]). In the absence of rotation, the film will eventually drip under the action of gravity. Moffatt showed that rotation prevents dripping if the angular velocity of the cylinder exceeds a threshold value that depends on the kinematic viscosity of the liquid, the radius of the cylinder and the acceleration owing to gravity. This is in line with everyday experience: we can prevent honey from dripping off a spoon by rotating the spoon. However, it is tricky to rotate the spoon continuously at a constant rate, and in practice one tends rather to twist it back and forth, endowing the spoon with a time-dependent angular velocity.

Working on the basis of lubrication theory, Moffatt [1] derived a nonlinear model equation for the film thickness and showed that it has a steady solution if the aforementioned threshold criterion is met. Working around the same time, Pukhnachev [4] derived a more general version of the governing equation that incorporated the effect of surface tension, and also demonstrated the existence and uniqueness of a steady solution. The steady solution describes a film profile which is stationary in the laboratory frame. Assuming counterclockwise rotation, the film exhibits a bulge in thickness on the right-hand side of the cylinder and is thinner on the left-hand side (see figure 1). Moffatt [1] also described the results of experiments that revealed the importance of transverse instability, which manifests as a sequence of liquid lobes spaced out along the axis of the cylinder.

Numerous papers have followed, examining various aspects of a problem that has proved to be very rich from a dynamics perspective. Hinch & Kelmanson [5] used asymptotic methods to show that surface perturbations decay and drift over a four time-scale cascade. Hinch *et al.* [6] probed these results further, focusing on shock formation in the zero surface-tension case and providing an estimate of the shock formation time. Hansen & Kelmanson [7] used a boundary integral formulation to compute surface profiles under conditions of Stokes flow, allowing for films of arbitrary thickness and including surface tension. Peterson *et al.* [8] carried out a comprehensive linear stability analysis and revealed the parameter regimes in which steady-state solutions are stable. Duffy & Wilson [9] analysed both attached films and curtain flows (for which a film falls onto the cylinder from above, curves around, and falls off the bottom), developed

analytical approximations and identified critical flow transitions. Evans *et al.* [10,11] presented both two- and three-dimensional models for coating flow on a rotating cylinder. Noakes *et al.* [12] examined the film stability to three-dimensional modes in the absence of gravity. Lopes *et al.* [13] introduced a new model equation, derived on the basis of Onsager's variational principle, which includes the full expression for the surface curvature in the capillary stress term. These authors also compared the model predictions for steady flow with full computations of the Stokes equations. Kelmanson [14] extended the Moffatt–Pukhnachev model to include the effect of inertia. Noakes *et al.* [15] used the method of multiple scales to analyse inertial effects for three-dimensional flows. Wray & Cimpeanu [16] used reduced-order techniques to incorporate thick films with inertia. Karabut [17] explored two distinct flow regimes depending on the angular velocity and allowing for the effect of surface tension. Gorla [18] examined the rupture dynamics of non-Newtonian power-law films.

Weak solutions exhibiting shocks were first introduced for the steady Moffatt–Pukhnachev flow by Johnson [19]; see also Badali *et al.* [20] and Benilov *et al.* [21]. Such solutions allow the cylinder to support a greater liquid volume than the smooth Moffatt solutions [1]. The stability of these weak solutions was studied by O'Brien [22] and Villegas-Díaz *et al.* [23], who demonstrated that stable configurations occur only when the shock is located in the fourth quadrant of the plane.

The problem of rimming flow, in which the liquid film coats the inside of the cylinder, is also of interest. As highlighted by Lopes [24], the thin-film equations for rimming flow and for the exterior flow problem are identical up to a certain order of approximation in the film thickness parameter, although key differences appear at higher order. Johnson [19] presented an analysis of steady-state coating flows inside rotating horizontal cylinders. O'Brien & Gath [25] identified the formation and position of shocks in rimming flows, addressing the occurrence of sharp transitions in film thickness. O'Brien [22] further contributed a linear stability analysis of rimming flows, describing conditions under which small disturbances may be amplified. The effect of inertia on rimming flow was incorporated by Benilov & O'Brien [26] and Benilov & Lapin [27]. Villegas-Diaz *et al.* [23,28] examined the stability of rimming flows to two-dimensional perturbations, combining analytical and numerical techniques and exploring the effect of surface shear on flow stability.

The present paper is devoted to the study of a viscous liquid film that coats the outside of a horizontal cylinder which rotates at a constant rate onto which are superimposed oscillations of a certain amplitude and frequency. We assume that the thickness of the liquid film is everywhere much smaller than the radius of the cylinder and employ lubrication theory to derive a generalization of the Moffatt–Pukhnachev equation, which incorporates a time-dependent modulation to the rotation rate. Although we discuss the subsequent dynamics in the context of the film coating the exterior of the cylinder, the aforementioned equivalence (up to some order in the film thickness parameter) between this and the rimming flow problem means that our observations are equally valid for rimming flow.

The paper is organized as follows. In §2, we derive the thin-film equation that forms the basis of our model. In §3, we briefly review the Moffatt–Puckhnachev flow for constant rotation, taking a dynamical system perspective. In §4, the dynamical system formed from the characteristic equations of our model equation is studied and discussed. In §5, we present solutions to the model equation and study the asymptotic limits of high- and low-frequency oscillations. Finally, in §6, we summarize our results.

2. Problem statement

We consider the flow of a liquid film of viscosity μ and density ρ that coats the exterior of a circular cylinder of radius a, as is illustrated in figure 1. The motion in the liquid is driven by the downwards force of gravity, which acts in the negative y direction, and by torsional rotations of the cylinder whose angular velocity is a prescribed periodic function of time, t. The flow is assumed to be two-dimensional in the xy-plane of the cylinder cross-section. The dynamics are described with reference to plane polar coordinates (r, θ) centred at the cylinder axis with $\theta = 0$

royalsocietypublishing.org/journal/rspa Proc. R. Soc. A 482: 20250748

aligned with the horizontal. Using thin-film theory Pukhnachev [4] and Moffatt [1] derived an equation for the film thickness when the cylinder rotates at a constant speed. Our first goal is to derive a modified version of this equation which accounts for a general angular velocity of the cylinder.

We define the dimensionless thin-film coordinate, ζ, such that

$$r = a(1 + \epsilon\zeta), \tag{2.1}$$

where $\epsilon = (\mu\Omega_*/\rho g a)^{1/2}$. Here, g is the acceleration owing to gravity and Ω_* is a reference angular velocity. The film surface is located at $\zeta = h(\theta, t)$, where h is to be found. In the sequel, it will be assumed that $\epsilon \ll 1$ so that the average film thickness, which is on the order of ϵa, is small in comparison with the cylinder radius, a. The velocity (u, v) in the (r, θ) directions, the pressure pe and time t are non-dimensionalized by making the replacements

$$u \mapsto \epsilon a\Omega_* u, \quad v \mapsto a\Omega_* v, \quad p \mapsto \epsilon^{-2}(\mu\Omega_*)p \quad \text{and} \quad t \mapsto \Omega_*^{-1} t. \tag{2.2}$$

To leading order in ϵ the dimensionless Navier–Stokes equations are

$$0 = p_\zeta, \quad 0 = -p_\theta - \cos\theta + v_{\zeta\zeta} \quad \text{and} \quad 0 = u_\zeta + v_\theta. \tag{2.3}$$

The inertia terms have been neglected in these equations. Defining the Reynolds number $Re = \rho\Omega_* a^2/\mu$, this is justified provided that $Re \ll \epsilon$ or, equivalently, $a\Omega_*^2/g \ll 1$.

At the film surface, $\zeta = h(\theta, t)$, we impose the kinematic condition at leading order,

$$h_t + v h_\theta - u = 0, \tag{2.4}$$

as well as the normal and tangential stress conditions

$$p = 0 \quad \text{and} \quad v_\zeta = 0, \tag{2.5}$$

respectively. The pressure in the air outside of the film has been taken to be zero. Moreover the contributions of both the viscous normal stress and the capillary stress in the first condition in equations (2.5) have been neglected. Neglecting the viscous normal stress requires that $\epsilon \ll 1$, which has already been assumed. Dropping the capillary stress is justified if $C \gg \epsilon^3$, where the capillary number $C = \mu\Omega_* a/\gamma$ with γ the coefficient of surface tension, and this is assumed henceforth. The boundary condition on the cylinder, $\zeta = 0$, is

$$u = 0 \quad \text{and} \quad v = \Omega(t), \tag{2.6}$$

where $\Omega(t)$ is assumed to take the form

$$\Omega(t) = 1 + b\cos\sigma t \tag{2.7}$$

for given constants $b > 0$ and $\sigma > 0$. If $b = 0$ then the cylinder is rotating at a constant rate; this is the case originally studied by Moffatt and Pukhnachev and we shall henceforth refer to it as the MP problem.

It would appear, then, that there are two relevant time scales in the problem: first, there is the time taken for a fluid particle to complete one circuit of the cylinder under steady rotation, i.e. for the MP problem which has a steady flow solution [1] and, second, there is the time scale associated with the modulational frequency σ.

Integrating the governing equations (2.3), applying the boundary conditions (equation (2.5) and equation (2.6)), and inserting the resulting expressions into the kinematic condition equation (2.4), we obtain the evolution equation

$$h_t + Q_\theta = 0, \tag{2.8}$$

where

$$Q = \int_0^h v\,\mathrm{d}\zeta = \Omega(t)h - \frac{1}{3}h^3\cos\theta \tag{2.9}$$

is the dimensionless flux in the film. The initial condition is

$$h(\theta, 0) = h_0(\theta) \tag{2.10}$$

for some appropriate choice of the function h_0.

In summary, we aim to solve equation (2.8) with initial condition equation (2.10) to determine the surface profile $h(\theta, t)$ for different choices of the parameters b and σ. Before doing this, however, it is instructive to recall the salient details of the steady flow for the MP problem. We do this in the next section from a dynamical systems perspective which provides a novel and intuitive way of visualizing the solution space.

3. The steady Moffatt–Pukhnachev flow

The steady MP problem is recovered by setting $b = 0$ so that the cylinder is rotating at a constant rate. Although it is strictly equal to unity in this case, we find it convenient to retain Ω in the relevant equations to facilitate later discussion. The governing equation (2.8) is

$$h_t + \left(\Omega h - \frac{1}{3}h^3 \cos\theta\right)_\theta = 0, \tag{3.1}$$

with initial condition given by equation (2.10). Moffatt [1] showed that, if a certain criterion is met, there exists a steady solution describing a fully attached film. Integrating the steady version of equation (3.1) with respect to θ, we obtain

$$\Omega h - \frac{1}{3}h^3 \cos\theta = Q, \tag{3.2}$$

where Q coincides with its definition in equation (2.9) and is herein constant. The constant Q level curves for equation (3.2) are shown in the phase portrait in figure 2. Critical to note in this figure is the separatrix curve, shown with a solid gold line, which divides level curves that correspond to physical, fully attached solutions (those below the solid gold curve) from those that correspond to unphysical solutions (those above it) for which h blows up; in the latter case the blow-up has the local form $h \sim a|\theta_c - \theta|^{-1/2}$ for constant a, where $\theta_c = -\pi/2$ or $\pi/2$. Solutions with shocks, which include sections of level curves above and below the solid separatrix, are also possible and have been discussed by previous workers (e.g. Johnson [19], O'Brien & Gath [25]). We touch upon these later for the case $b > 0$.

A parametric description of the level curves is obtained by solving the characteristic equations for equation (3.1), namely,

$$\frac{\mathrm{d}h}{\mathrm{d}\tau} = -\frac{1}{3}h^3 \sin\theta, \quad \frac{\mathrm{d}\theta}{\mathrm{d}\tau} = \Omega - h^2 \cos\theta \equiv M(\theta) \quad \text{and} \quad \frac{\mathrm{d}t}{\mathrm{d}\tau} = 1, \tag{3.3}$$

where the independent variable τ varies continuously along a characteristic. It is straightforward to check that equation (3.2) is a first integral of equation (3.3). We define the period $P(Q)$ of a steady orbit to be the time taken for θ to change by 2π radians. By integrating the second formula in equation (3.3), we find

$$P(Q) = \int_0^{2\pi} \frac{1}{\Omega - h^2 \cos\theta}\, \mathrm{d}\theta. \tag{3.4}$$

This fixes a base frequency associated with the steady flow, given by $\omega^*(Q) = 2\pi/P(Q)$. The dependence of ω^* on Q is graphed in figure 3b where it can be seen that $\omega^* \in [0, 1]$ and it is monotone decreasing in Q. We note the limits $\omega^* \to 1$ ($P \to 2\pi$) as $Q \to 0$, and $\omega^* \to 0$ ($P \to \infty$) as $Q \to Q^*$, that is, as the separatrix in figure 2 is approached.

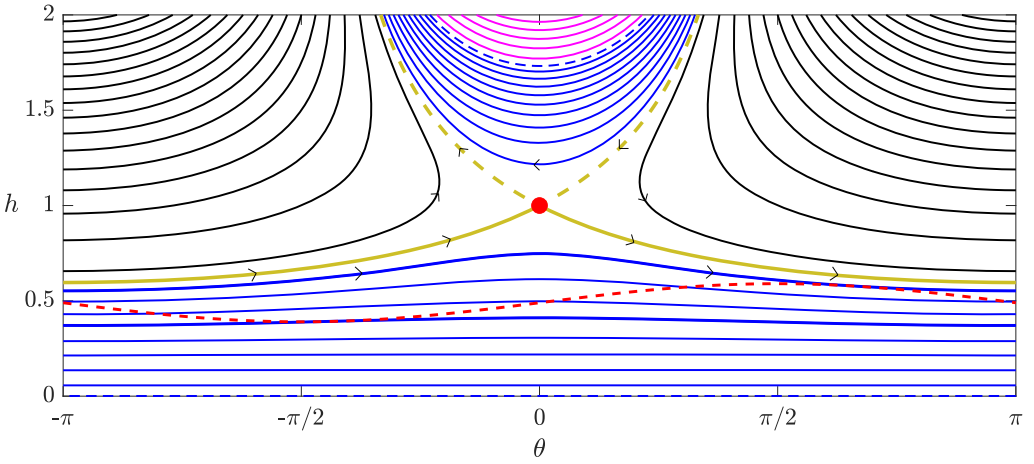

Figure 2. One period, $\theta \in [-\pi, \pi)$, of the phase portrait for the system equation (3.3) corresponding to the steady MP problem with $\Omega = 1$ ($b = 0$). Each trajectory is described by equation (3.2) and corresponds to a particular value of Q. Black lines show $Q > 2/3$, blue lines show $0 < Q < 2/3$, and magenta lines show $Q < 0$. The blue dashed lines indicate $Q = 0$. The separatrix, shown with a thick gold line (both solid and dashed), corresponds to $Q = Q^* = 2/3$; the solid part delineates the boundary between regular solutions to the characteristic equations (3.3) and those exhibiting finite-time blow-up. The minimum value of h along the separatrix occurs at $\theta = \pm\pi$ and is $h_{\min} = p^{1/3} - 1/p^{1/3} \approx 0.5961$, where $p = 1 + \sqrt{2}$. The red dots indicate the location of the saddle points for equation (3.3), and the arrows on the trajectories indicate the direction of travel as τ increases. The broken red line indicates a typical initial film profile, $H(\theta)$, bounded by envelope trajectories shown with thick blue lines.

Viewed as a two-dimensional dynamical system equation (3.3) has a saddle point at $(h, \theta) = (1, 0)$. Its stable and unstable manifolds are the level curves of equation (3.2) with $Q = Q^*$, where

$$Q^* = \frac{2}{3}\Omega^{3/2}. \tag{3.5}$$

They are shown with solid gold and dashed gold lines in figure 2. An initial condition for equation (3.3) at $\tau = 0$ which corresponds to a point (h, θ) lying beneath the solid separatrix will trace out a physically acceptable, fully attached solution for some $Q < Q^*$. The requirement that $Q \le Q^*$ coincides with the criterion given by Moffatt [1] for a steady solution, namely (explicitly here setting $\Omega = 1$),

$$\left(\frac{\rho g}{\mu a^3 \Omega_*^3}\right)^{1/2} \tilde{Q} < \frac{2}{3}, \tag{3.6}$$

where $\tilde{Q}$ is the dimensional flux, with $\tilde{Q} = \epsilon(a^2\Omega_*)Q$. Intuitively, we might expect that for time dependent forcing, i.e. $\Omega = \Omega(t)$ as given by equation (2.7), then blow-up will occur if the Moffatt criterion equation (3.6) is violated at some point during the time cycle. In fact the dynamics turn out to be more complex than this, as we shall see.

In figure 3a, we show the variation with the dimensionless flux Q of the dimensionless fluid volume,

$$V = \int_0^{2\pi} h(\theta)\, \mathrm{d}\theta. \tag{3.7}$$

The plot assumes a smooth solution with no shocks. The maximum volume, attained when $Q = Q^*$, is given by

$$V^* = 12\Omega^{1/2} \int_{\hat{h}_m}^{1} \frac{\mathrm{d}x}{(x+2)^{1/2}(x^3 + 3x - 2)^{1/2}}, \tag{3.8}$$

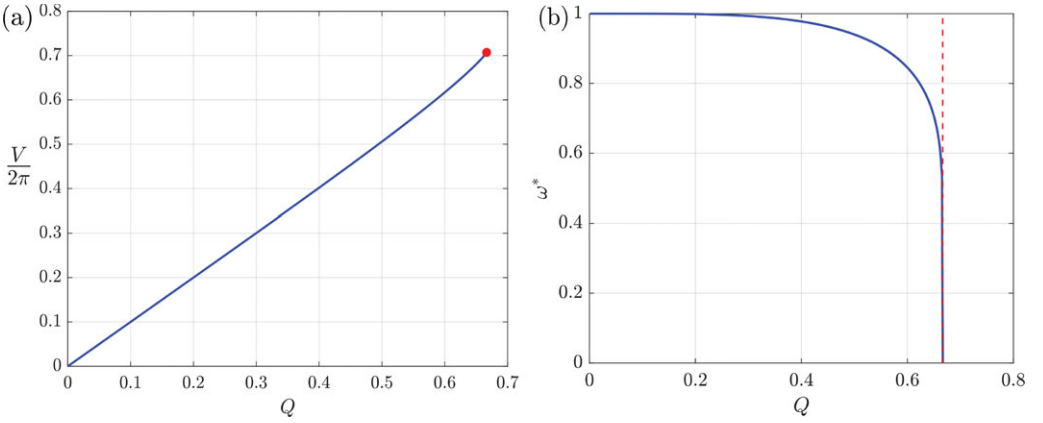

Figure 3. (a) The scaled fluid volume, $V/(2\pi)$, plotted against Q. The red dot indicates the limiting steady volume that obtains at the separatrix in figure 2 when $Q = 2/3$. (b) The dependence $\omega_*(Q)$ for the MP problem equation (3.1). The base frequency, ω^*, is related to the period $P = 2\pi/\omega^*$, being the time taken for a point $(\theta(\tau), h(\tau))$ obeying equation (3.3) to complete one 2π-period in θ of a fixed-Q trajectory in the phase plane shown in figure 2.

where $\hat{h}_m$ is the minimum value of $h/\Omega^{1/2}$, which occurs at $\theta = \pm\pi$. In the case of $\Omega = 1$, $\hat{h}_{\min} = p^{1/3} - 1/p^{1/3} \approx 0.5961$, where $p = 1 + \sqrt{2}$. The integral equation (3.8) can be calculated exactly but the resulting expression in terms of elliptic integrals is unwieldy and is not included here. Numerically we calculate $V^*/(2\pi\Omega^{1/2}) \approx 0.70708140$, which agrees with the value quoted by O'Brien & Gath [25].

If at $t = 0$ the starting profile $h_0(\theta)$ in the initial condition equation (2.10) coincides with one of the phase plane trajectories with $Q \le Q^*$ in figure 2, $H(\theta)$, say, then $h(\theta, t) = H(\theta)$ for all $t \ge 0$. Consider instead a starting profile h_0 that does not coincide with a steady solution such as that shown with a dashed red line in figure 2. If all or part of the profile crosses the solid gold separatrix then $h(\theta, t)$ will blow up at a finite-time singularity. Assume that $h_0(\theta)$ is everywhere underneath the solid gold separatrix. Then $h(\theta, t)$ will be confined between the two osculating trajectories which are just tangent to the maximum and minimum of h_0 (these trajectories are shown with heavier solid blue lines in figure 2). This is clear since each point on the initial profile h_0 must traverse one of the level curves sandwiched between the two osculating curves. Since the period P increases with Q (see figure 3b), points following trajectories for lower Q tend to catch up with those following trajectories for larger Q, and steepening of the wave profile occurs leading to a discontinuity in the film thickness (Moffatt [1]). This heralds the onset of film overturning and shock formation, a phenomenon captured by the analysis of Hinch *et al.* [6].

For the time-dependent problem we note that, with Ω constant, equation (2.8) possesses an infinite set of conserved quantities. We fix $\Omega = 1$ and define, for integer $n \ge 0$, $\chi_n = \int Q^n dh$, where Q is defined in equation (2.9) and where we treat h and θ as being independent in the integration. Then $\chi_n^* = \int_0^{2\pi} \chi_n \, \mathrm{d}\theta$ is a conserved quantity for equation (2.8). To see this, differentiate χ_n^* with respect to t and use the fact that $h_t = -Q_\theta$ and the 2π-periodicity of Q in θ. The case $n = 0$ corresponds to volume conservation, but $n \ge 1$ does not have an obvious physical interpretation. We also note that with Ω constant equation (2.8) can be put into the Hamiltonian form

$$h_t + \frac{\partial}{\partial\theta}\left(\frac{\delta\chi_1^*}{\delta h}\right) = 0, \tag{3.9}$$

where $-\chi_1^*$ plays the role of the Hamiltonian.

(a) Stability of the steady solution

The linear stability of the steady solutions described above for constant Ω has been discussed by O'Brien [22] for rimming flow, and the same analysis carries over here. We review briefly the essential details as these will prove useful in the ensuing analysis.

Writing $h = h_s(\theta) + \eta(\theta, t)$, where $h_s(\theta)$ is a steady solution of the MP problem for $Q < Q^*$, and $\eta(\theta, t)$ is a small perturbation, we substitute into equation (3.1). Neglecting higher-order terms,

$$\eta_t + (M_s \eta)_\theta = 0, \tag{3.10}$$

where $M_s(\theta) = \Omega - h_s^2 \cos\theta$ and, we emphasize, Ω is constant. Assuming that $Q < Q^*$ it is straightforward to show that $M_s > 0$ (see appendix A).

Since the coefficients in equation (3.10) are 2π-periodic in θ, we can use Floquet theory to justify writing $\eta = \mathrm{e}^{\mathrm{i}\omega t} f(\theta) + \text{c.c.}$, where c.c. means complex conjugate, and where the 2π-periodic in θ function $f(\theta)$ and the constant ω are to be found. Substituting into equation (3.10), and integrating, we find $f(\theta) = c\psi(\theta)$ for arbitrary constant c, where

$$\psi(\theta) = \frac{1}{M_s}\, \mathrm{e}^{-\mathrm{i}\omega \nu(\theta)}, \quad \nu(\theta) \equiv \int_\pi^\theta \frac{\mathrm{d}\xi}{M_s(\xi)}. \tag{3.11}$$

The integrand in equations (3.11) can be expressed as the Fourier series $1/M_s(\xi) = \sum_{n=-\infty}^{\infty} a_n \exp(\mathrm{i}n\xi)$ with $a_n = \bar{a}_{-n}$. The zeroth mode has $a_0 = P(Q)/2\pi$, where $P(Q)$ was defined in equation (3.4). It is clear from equations (3.11) that the required periodicity of f is assured only if $\omega a_0 = m$ for $m \in \mathbb{N} \cup \{0\}$. Since a_0 is real it follows that ω is real and the MP solution is neutrally stable [22]. This neutral stability was also previously noted by Villegas-Díaz *et al.* [23], who used the method of characteristics to obtain the solution of equation (3.10),

$$\eta(\theta, t) = \frac{1}{\Omega - h_s^2 \sin\theta} U\left(t - \int_{\theta_0}^\theta \frac{\mathrm{d}\xi}{M_s(\xi)}\right), \tag{3.12}$$

where θ_0 is an arbitrary constant. The function U is set by the disturbance to the steady surface profile at $t = 0$. Villegas-Díaz *et al.* [23] also discussed the stability of the steady MP solution for the special case $Q = Q^*$.

The fact that linear perturbations are stable, taken together with the observation from the previous section that any perturbation from a steady solution will lead to a finite-time slope singularity, makes clear that nonlinearity plays an important role in the dynamics, even for arbitrarily small perturbations. In passing, we note that an extended form of equation (3.1) that incorporates higher-order terms in the lubrication approximation was derived by Benilov *et al.* [29] and was also shown to have neutrally stable steady solutions. Despite the neutrality of its eigenmodes, Benilov *et al.* [29] showed that the linearization of the extended equation about a steady state admits a so-called 'explosive instability': despite the linearized problem yielding an infinite number of bounded harmonic modes (which would normally be taken to imply stability) it supports explosive disturbances that blow up in finite time.

4. The characteristic dynamical system

In general a numerical approach is required to handle the case of a time-dependent angular velocity, $\Omega = \Omega(t)$. In this section we carry out a numerical investigation of the dynamical system equation (3.3) with $\Omega(t)$ given by equation (2.7). The problem may be put into the form of the time-periodically perturbed Hamiltonian system

$$\boldsymbol{J}\frac{\mathrm{d}\boldsymbol{u}}{\mathrm{d}t} = \nabla H_p + \boldsymbol{p}, \quad \boldsymbol{p} = \begin{pmatrix} -b\cos\sigma t \\ 0 \end{pmatrix} \quad \text{and} \quad \boldsymbol{J} = \begin{pmatrix} 0 & -1 \\ 1 & 0 \end{pmatrix}, \tag{4.1}$$

where $\boldsymbol{u} = (h, \theta)^T$ and $\nabla = (\partial_h, \partial_\theta)^T$. The Hamiltonian, H_p, is such that

$$-H_p = h - \frac{1}{3}h^3 \cos\theta. \tag{4.2}$$

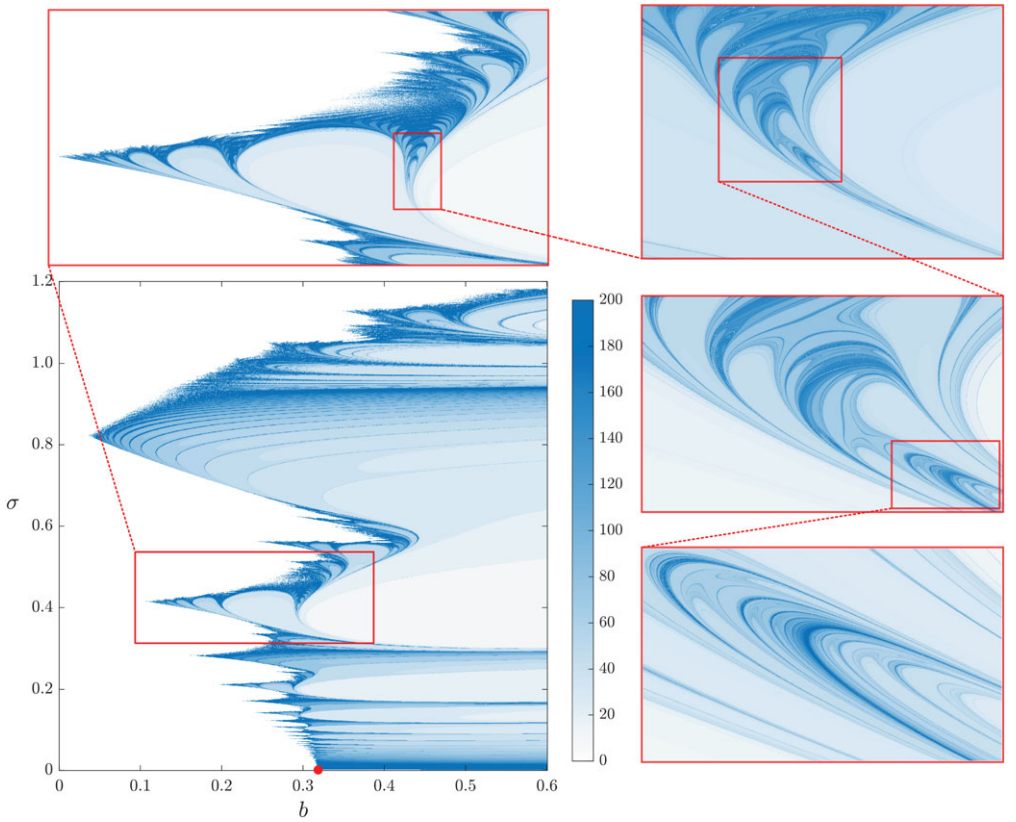

Figure 4. The blow-up map obtained by integrating the characteristic equations (3.3) with the initial condition equation (4.3) taking $h^* = 1/\sqrt{3}$, with $\Omega(t)$ given by equation (2.7). Points in the $b\sigma$-plane are coloured white if the solution remains bounded occurs and blue if blow-up occurs. The shade of blue is determined by the time at which blow-up occurs indicated in the colour bar: darker blue corresponds to later blow-up times. Here blow-up is deemed to have occurred when $h = 5.0$ is reached. The red marker point at $(\sigma, b) = (0, 0.317)$ indicates the predicted blow-up threshold from the small-σ analysis of §5b.

The form of $\Omega(t)$ is given in equation (2.7). When $b = 0$ the perturbation vanishes, $\boldsymbol{p} = \mathbf{0}$, and the system equation (4.1) is integrable. This corresponds to the steady flow MP problem discussed in §3.

To construct the film profile at time t, we could integrate equation (4.1) forwards in time from a discrete set of starting values $h(0), \theta(0)$ chosen to approximate a chosen initial profile. However, to help build intuition it is instructive to first view equation (4.1) as a standalone dynamical system and carry out a study of the dynamics for a single starting value. To do this we select the starting point

$$\theta = -\frac{\pi}{2} \quad \text{and} \quad h = h^* \tag{4.3}$$

at $t = 0$, and integrate equation (4.1) forwards in t numerically for a range of values of b and σ using the MATLAB routine *ode45*. In so doing we build up a map of the solution space, distinguishing between solutions that remain bounded and those that blow up in finite time. The latter is detected by testing when h exceeds a selected value. This is sufficient to give an accurate picture: blow-up is initiated when the solution trajectory of equation (4.1) latches onto the unstable manifold (leftmost dashed part of the gold separatrix in figure 2) and it occurs very rapidly thereafter and on a much shorter time scale than the time period of the cylinder oscillations. In our computations we deemed blow-up to have occurred when $h \geq 5.0$.

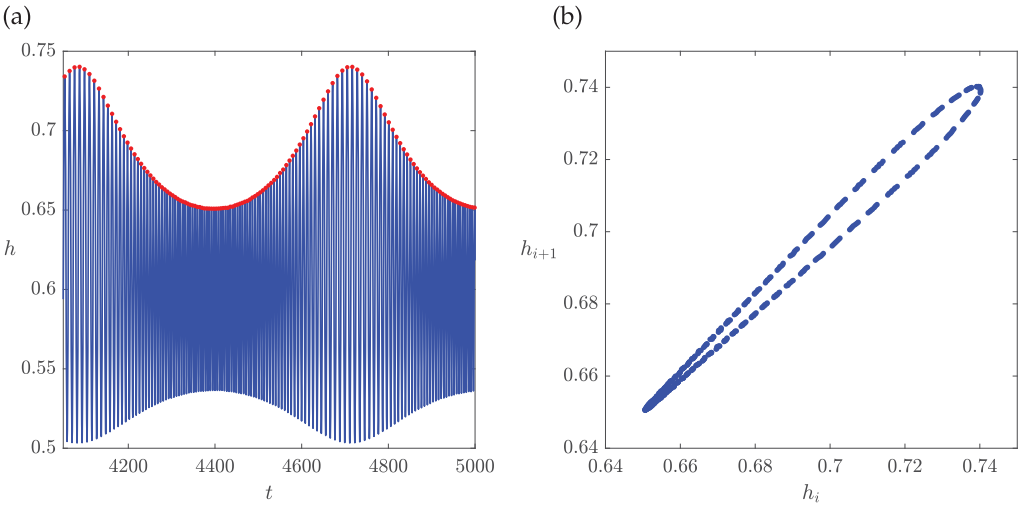

Figure 5. Integration at the point $(b, \sigma) = (0.25, 0.01)$ in figure 4 up to $t = 5000.0$. (a) Time signal over the later stages of the integration; the red markers indicate the local maxima. (b) The return map (h_i^m, h_{i+1}^m), where h_i^m is the ith local maximum of the time signal.

Figure 4 shows the behavioural map in the $b\sigma$-plane for $h^* = 1/\sqrt{3}$. The blue shading indicates the blow-up time with darker blue corresponding to later blow-up times. In the white region no blow-up was encountered in $0 \le t \le 3500$, and we take this to mean that the solution remains regular and bounded. Since the chosen h^* is below $Q^* = 2/3$, the solution at $b = 0$ traverses one of the level curves below the solid gold separatrix in figure 2 and is therefore bounded. The complexity of the map is apparent and some of the features are reminiscent of the complex structures created by discrete one-dimensional maps, including highly intricate boundaries and the emergence of apparent self-similarity upon zooming in to certain parts of the picture. The latter phenomenon is seen in the various subsidiary panels in figure 4.

The red marker point at $(\sigma, b) = (0, 0.317)$ indicates the threshold for blow-up predicted by the small-σ analysis to be discussed in §5b. When σ is small the solution is found to be quasiperiodic in nature. This is illustrated in figure 5 for the point $(b, \sigma) = (0.25, 0.01)$ in figure 4. The integration was carried out up to $t = 5000.0$. Panel (a) shows the time signal over the last 1000 time units, and panel (b) shows a return map with (h_i^m, h_{i+1}^m), where h_i^m is the ith local maximum of the time signal, shown with dots. The appearance of an almost complete closed loop in the return map is the classic hallmark of quasiperiodic dynamics (e.g. Guckenheimer & Holmes [30]).

A particularly interesting feature of the map is that there appears to be some sort of resonance manifesting as a sequence of sharp protrusions extending to the left-hand side. With $h^* = 1/\sqrt{3}$ the unforced oscillator (viz. equation (4.1) with $\boldsymbol{p} = \boldsymbol{0}$) has the natural frequency $\omega^*(1/\sqrt{3}) = 0.877$. The uppermost protrusion in figure 4 has its apex at a value of the forcing frequency, σ, that is close to this. Moreover, the various protrusions below occur at values of σ that are close to rational multiples of ω^*. The fact that these apparently resonant values of σ do not quite coincide with ω^* (or a rational multiple thereof) is presumably attributable to the nonlinearity of the underlying oscillator.

5. The Moffatt–Pukhnachev flow with periodic modulation

Since the original partial differential equation (2.8), for the cylinder flow problem is hyperbolic, the appearance of shocks is expected. Therefore, while indicative, the results of the previous section, which followed single-trajectory solutions of the Hamiltonian system equation (4.1), should be interpreted with some care in the context of the rotating cylinder problem. In this

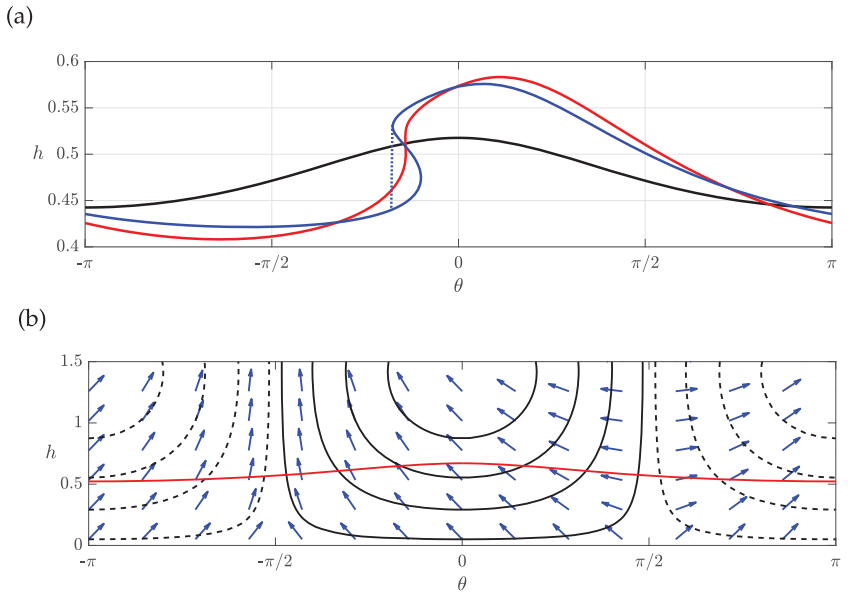

Figure 6. (a) Typical solution behaviour for the model equation (2.8) in the presence of modulation, here with $b = 0.25$ and $\sigma = 0.5$. The computation was carried out by solving the characteristic system equation (4.1) numerically using MATLAB routine ode45. The initial profile (black curve) $h_0 \in \mathcal{H}$ has $\mathcal{Q}_0 = \sqrt{2}/3$. The profile at the occurrence of the slope singularity at $t \approx 55.4$ is shown in red. The blue curve shows the film profile predicted by equation (4.1) at $t = 60$; the blue dotted line indicates how a shock could be introduced to interpret the profile as a single-valued solution of equation (2.8). (b) The strain and vorticity fields for the flow with streamfunction $\mathcal{H}_p$ given in equation (4.2). The arrows show the dominant eigenvector of the associated rate of strain tensor and the continuous lines show contours of constant positive (solid lines) and negative (dashed lines) vorticity. The solid red line shows a steady solution (see figure 2) solving equation (3.2) with $\Omega = 1$ and $Q = 0.57$.

section we study solutions to the initial value problem equations (2.8), (2.10) with $\Omega(t)$ given in equation (2.7). It will be important to distinguish between initial conditions that correspond to solutions of the equivalent instantaneous steady problem and those that do not. To this end we define the class of functions

$$\mathcal{H} = \{h(\theta) : \Omega_0 h - \frac{1}{3}h^3 \cos\theta = \mathcal{Q}_0 \text{ for some } \mathcal{Q}_0 \in [0, 2/3]\}, \tag{5.1}$$

where $\Omega_0 = \Omega(0) = 1 + b$. If we write $h = \Omega_0^{1/2} H$ and $\mathcal{Q}_0 = q_0 \Omega_0^{3/2}$, then the restriction in $\mathcal{H}$ reduces to $H - \frac{1}{3}H^3 \cos\theta = q_0$, contours of which correspond to solutions of the steady MP problem and are shown in figure 2.

Intuitively we might expect the $b \neq 0$ oscillations to cause the film surface to overturn and become multi-valued signifying the breakdown of equation (2.8). This is indeed the case, and for a general choice of modulation frequency σ and amplitude b the solution $h(\theta, t)$ develops an infinite slope singularity at some time $t^* > 0$. Sample profiles are shown in figure 6 for the case $\mathcal{Q}_0 = \sqrt{2}/3$ (black curve) taking $b = 0.25$ and $\sigma = 0.5$. The numerical computations were carried out by integrating the characteristic system equation (4.1) forward in time from the starting profile using the MATLAB routine *ode45*. A parametric representation is introduced in which $(\theta(\xi_i, t), h(\xi_i, t))$ is tracked in time for $i = 1, \ldots, N$, where ξ_i is one of N equally spaced points in the range $[0, 2\pi)$. The onset of overturning is detected by monitoring if there is a sign change in θ_ξ, the differentiation in ξ being done with spectral accuracy using a fast Fourier transform. Typically we found that using a grid with 128 equally spaced points in ξ is sufficient to get an accurate solution; the MATLAB integrator *ode45* uses an adaptive time step that, in the results to be presented, typically varies between 10^{-3} and 10^{-5}.

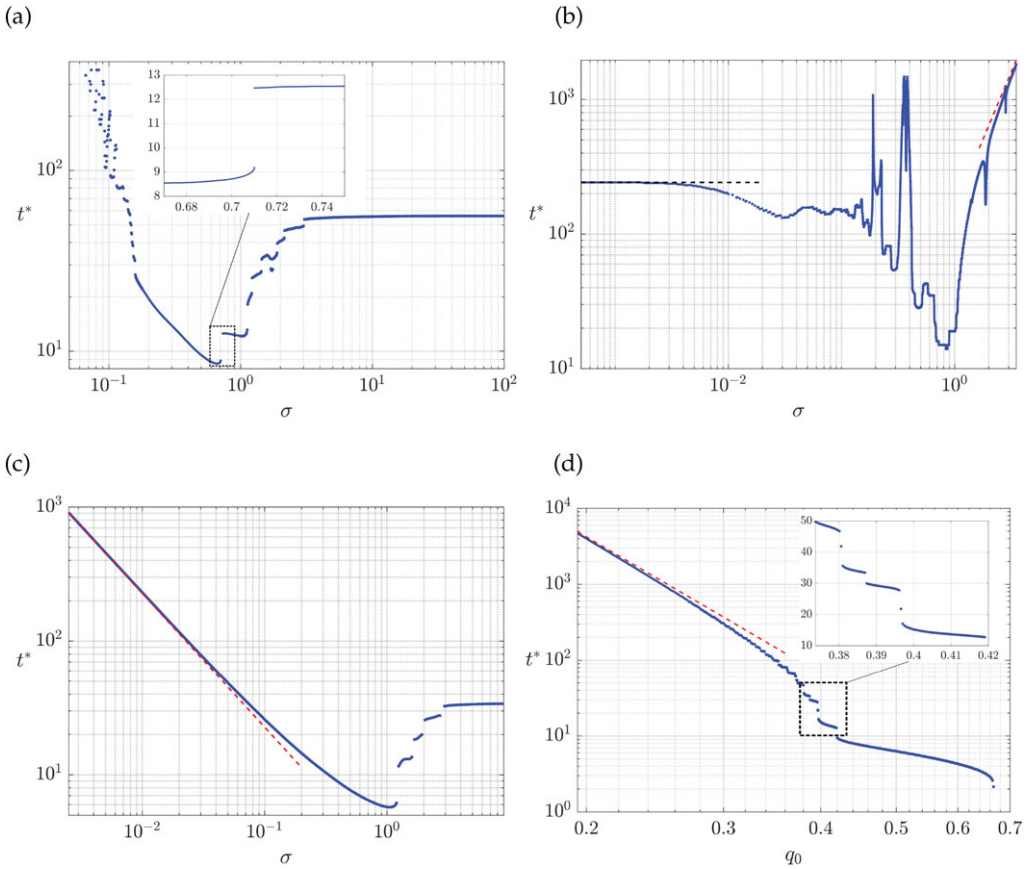

Figure 7. The overturning time, t^*, shown against modulation frequency σ, for the governing equation (2.8) with initial condition equation (2.10) and starting profile h_0. (a) $b = 0.3, h_0(\theta) \in \mathcal{H}$ with $\mathcal{Q}_0 = q_0\Omega_0^{3/2}, q_0 = 0.5$, (b) $b = 0.3, h_0 \notin \mathcal{H}$ solving $h_0 - (1/3)h_0^3 \cos\theta = 1/2$, and (c) $b = 0.5, h_0 \in \mathcal{H}$ with $\mathcal{Q}_0 = q_0\Omega_0^{3/2}, q_0 = \sqrt{2}/3 = 0.471$. For (a) the point $(b, q_0) = (0.3, 0.5)$ lies in the white region in figure 10 corresponding to a regular asymptotic solution in the small-σ limit (refer to §5b). In (b) the black dashed line indicates the overturning time obtained by integrating equation (5.16) with $\Omega(T)$ frozen at Ω_0; the red dashed line shows the curve $t^* = 160\sigma^{-2}$, the coefficient having been chosen to obtain a reasonable fit. In (c) the point $(b, q_0) = (0.5, 0.471)$ lies in the blue blow-up region in figure 10, and the red dashed line shows the curve $t^* = T_s^*\sigma^{-1}$, where $T_s^* = 2.270$ is computed by integrating equation (5.26) subject to $q(0) = \sqrt{2}/3$. (d) The overturning time t^* versus q_0 for $b = 0.5$ and $\sigma = 0.6$. The initial condition is equation (2.10) with $h_0 \in \mathcal{H}$ and $\mathcal{Q}_0 = q_0\Omega_0^{3/2}$, where $\Omega_0 = \Omega(0)$; the red dashed line shows the curve $t^* = 0.27q_0^{-6}$, the coefficient having been chosen to obtain a reasonable fit.

In figure 7a–c we show how the overturning time t^* varies with σ for two cases chosen so that $h_0 \in \mathcal{H}$ in one and $h_0 \notin \mathcal{H}$ in the other. The modulation amplitude is set at $b = 0.3$. The asymptotic results shown in this figure are discussed in a later section. It is quite striking, particularly in figure 7a, that the $t^*(\sigma)$ curve exhibits numerous jump discontinuities. The presence of these discontinuities has been confirmed by meticulous numerical computations, including a very careful convergence study using up to $N = 1024$ points in ξ and a time step of size 10^{-5}.

To explain the jump discontinuities, and with reference to the system equation (4.1), we regard the Hamiltonian $H_p(\theta, h)$ given in equation (4.2) as the stream function for a two-dimensional incompressible fluid flow in the θh-plane. In this interpretation the flow occupies the whole plane and is not confined to the domain of the liquid for the cylinder problem. Solving equation (4.1) elicits the trajectories of individual particles advected passively within this flow, with the liquid surface corresponding to a material line. As it moves with the flow, this material line is stretched

and distorted by the flow's strain and vorticity fields. These fields, which are independent of time, are illustrated in figure 6b: the arrows show the direction of dominant strain corresponding to the eigenvector of the rate of strain tensor with positive eigenvalue (we recall that since the rate of strain tensor is symmetric, its two eigenvalues, which are real, sum to zero, and its two eigenvectors are mutually orthogonal). In general, material elements tend to align with the dominant strain eigenvector whilst being rotated one way or another according to the sign of the vorticity. The constant vorticity contours are solid where the vorticity is positive, promoting counterclockwise rotation, and dashed where the vorticity is negative, promoting clockwise rotation. For $b = 0$ a steady solution has a surface profile that stays fixed as the competitive effects of strain and rotation are in perfect balance; see the solid red line in figure 6b.

Certain parts of the strain-vorticity field promote steepening of the material surface and others promote flattening. The region around $\theta = -\pi/2$ presents a particular danger zone for surface steepening. Here the magnitude of the vorticity is small and the dominant strain eigenvectors are almost vertical. In contrast, the region around $\theta = \pi/2$ has weak vorticity and almost horizontal strain vectors, and therefore this region strongly encourages flattening of the surface. It appears that we get a jump discontinuity in t^* at a certain σ because, just below this frequency, the surface overturns near to $\theta = -\pi/2$; but for a slightly larger σ the overturning is just avoided and the surface must travel a further distance through a less dangerous region before overturning is finally induced in the danger zone some time units later.

In figure 7d, we show the overturning time t^* for the case $b = 0.5$ and $\sigma = 0.6$ and for a range of different initial conditions. The latter are given by equation (2.10) with $h_0 \in \mathcal{H}$ and $\mathcal{Q}_0 = q_0 \Omega_0^{3/2}$. The panel shows t^* plotted against q_0, and we see the occurrence of jump discontinuities at certain values of q_0. Some of these are highlighted in the inset. Since $q_0 \to 0$ corresponds to taking an initial profile that is close to the wall and almost flat (see figure 2), we expect the overturning time to diverge in this limit. The dashed red line in figure 7d suggests that this is indeed what occurs and, moreover, it happens such that $t^* \sim q_0^{-6}$.

To further understand the dynamics it is instructive to consider the flow in the high-frequency ($\sigma \gg 1$) and low-frequency ($\sigma \ll 1$) limits. These are examined in the following subsections.

(a) High-frequency limit ($\sigma \gg 1$)

Our numerical results suggest that the flow is periodic in time if σ is sufficiently large, and this motivates an investigation of the dynamics when $\sigma \gg 1$. In this limit there are two naturally disparate time scales in the problem: an $O(1)$ time scale associated with the steady part of Ω, that is, the continuous rotation, and an $O(1/\sigma)$ time scale associated with the rapid superimposed oscillations. Having said this, we might intuit that for an initial condition corresponding to a steady Moffatt–Pukhnachev solution, the former time scale is essentially removed and the flow will develop on time scales of the rapid oscillation.

Keeping the preceding comments in mind, we perform a multiple-scales analysis incorporating both time scales. Let $h = h(\theta, t, T)$ with $T = \sigma t$ acting as the fast time variable and t acting as the slow time variable. Assuming in the usual way that t and T are independent equation (2.8) becomes

$$h_t + \sigma h_T + \left(\Omega(T) h - \frac{1}{3} h^3 \cos\theta \right)_\theta = 0, \tag{5.2}$$

where $\Omega(T) = 1 + b \cos T$. We expand by writing

$$h(\theta, t, T) = h_0(\theta, t, T) + \sigma^{-1} h_1(\theta, t, T) + \sigma^{-2} h_2(\theta, t, T) + \sigma^{-3} h_3(\theta, t, T) + O(\sigma^{-4}). \tag{5.3}$$

Introducing this expansion into equation (5.2), at leading order, $O(\sigma)$, we find that $h_{0T} = 0$, which implies $h_0 = h_0(\theta, t)$. At order $O(1)$ we obtain $h_{1T} = -b h_{0\theta} \cos T - F(\theta, t)$, where

$$F(\theta, t) = h_{0t} + \left(h_0 - \frac{1}{3} h_0^3 \cos\theta \right)_\theta. \tag{5.4}$$

royalsocietypublishing.org/journal/rspa Proc. R. Soc. A 482: 20250748

Integrating with respect to T,

$$h_1(\theta,t,T) = -bh_{0\theta}\sin T - F(\theta,t)T + A_1(\theta,t), \tag{5.5}$$

where $A_1(\theta,t)$ is an arbitrary function of integration. In order to avoid secular terms, we demand that $F=0$. Then the leading-order term h_0 satisfies the original equation (2.8) with constant unit forcing frequency, $\Omega=1$, that is, it corresponds to a solution of the constant rotation rate MP problem. To prevent $h_0(\theta,t)$ from developing a slope singularity (a possibility discussed in §3), we take $h_0 \equiv h_s(\theta)$, where the steady solution h_s satisfies equation (3.2) with $\Omega=1$ for some flux $Q<2/3$.

Proceeding, we have

$$h_1(\theta,t,T) = -bh_{0\theta}\sin T + A_1(\theta,t). \tag{5.6}$$

At order $O(\sigma^{-1})$,

$$h_{2T} = -h_{1t} - ((\Omega(T) - h_0^2\cos\theta)h_1)_\theta. \tag{5.7}$$

Substituting equation (5.6) into the right-hand side of equation (5.7), we see that secular terms in h_2 will not arise if the T independent terms vanish, that is, if

$$A_{1t} + (\mathcal{M}A_1)_\theta = 0, \tag{5.8}$$

where $\mathcal{M} = 1 - h_0^2\cos\theta$. This is the same as the equation that governs the linear stability of the MP problem, namely, equation (3.10). Since h_0 has been chosen to be a steady solution of the MP problem, according to the results of §3a, A_1 is t-periodic with frequency $\omega = m/a_0$, where a_0 is given in §3a and $m \in \mathbb{N}\cup\{0\}$. Hence we have

$$A_1(\theta,t) = \lambda e^{i\omega t}\psi(\theta) + \text{c. c.}, \tag{5.9}$$

where λ is an arbitrary constant. The 2π-periodic function $\psi(\theta)$ was given in equation (3.11).

Integrating equation (5.7),

$$h_2 = -\frac{1}{4}b^2h_{0\theta\theta}\cos 2T - b(\mathcal{M}h_{0\theta})_\theta\cos T - bA_{1\theta}\sin T + A_2(\theta,t), \tag{5.10}$$

where $A_2(\theta,t)$ is an arbitrary function of integration. At order $O(\sigma^{-2})$

$$h_{3T} = -h_{2t} - ((\Omega(T) - h_0^2\cos\theta)h_2 - h_0h_1^2\cos\theta)_\theta. \tag{5.11}$$

The secularity condition requiring that the T-independent terms on the right-hand side of equation (5.11) be eliminated takes the form

$$A_{2t} + (\mathcal{M}A_2)_\theta = \frac{dS}{d\theta} + \lambda^2 e^{2i\omega t}(\psi^2h_0\cos\theta)_\theta + \text{c .c.}, \tag{5.12}$$

where

$$S(\theta) = \frac{1}{2}b^2(h_0(h_0h_{0\theta})_\theta\cos\theta - h_{0\theta\theta} - h_0^2h_{0\theta}\sin\theta). \tag{5.13}$$

We seek a solution in the form $A_2(\theta,t) = \alpha_{20}(\theta) + e^{2i\omega t}\alpha_{22}(\theta) + \text{c. c.}$, with α_{20} and α_{22} required to be 2π-periodic in θ. It is clear from equation (5.12) that $\alpha_{20}(\theta)$ has this property. Solving for $\alpha_{22}(\theta)$ using an integrating factor, we find that it is 2π-periodic if

$$\lambda^2\int_0^{2\pi}(\psi^2h_0\cos\theta)_\theta(\psi\mathcal{M})^2\,d\theta = 0. \tag{5.14}$$

This holds if $\omega=0$ (so that $\psi \propto 1/\mathcal{M}$) in which case $A_1 = \kappa_1/\mathcal{M}(\theta)$ and $A_2 = (S(\theta)+\kappa_2)/\mathcal{M}(\theta)$ for arbitrary constants κ_1 and κ_2. Thus the slow time-scale t-dependence drops out to the current order of approximation, as was anticipated.

In the light of the preceding discussion, and recognizing that the first term on the right-hand side of equation (5.6) represents a translation in θ by an amount $\sigma^{-1}\Omega_T$, we may now revise the

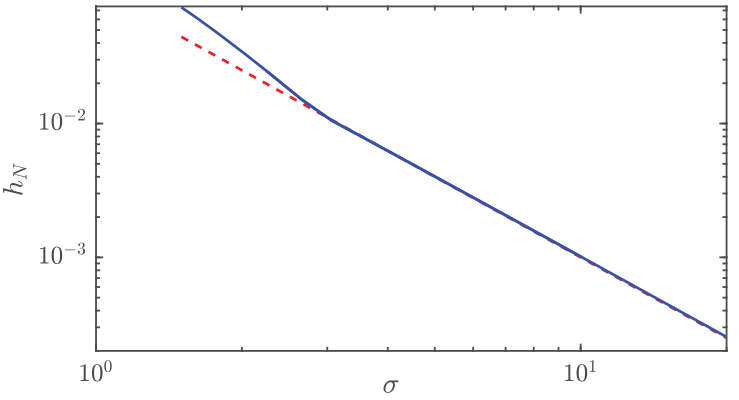

Figure 8. Log–log plot of the norm h_N (blue solid line) defined to be the maximum value of $h(\theta,t) - h_s(\theta + \sigma^{-1}\Omega_T)$ over $\theta \in [0, 2\pi)$ during the time period $t \in [0, 10/\sigma]$ (here $T = \sigma t$). The function $h(\theta,t)$ was computed by solving equation (4.1) numerically with the initial profile $h(\theta, 0) = h_s(\theta)$, where $h_s(\theta)$ solves equation (3.2) with $\Omega = 1$ and $Q = 0.5$. The modulation amplitude $b = 0.2$. A best fit curve $h_N = 0.1/\sigma^2$ is shown with a dashed red line.

expansion equation (5.3) to read

$$h(\theta, t, T) = h_s(\theta + \sigma^{-1}\Omega_T) + \sigma^{-1}\frac{\kappa_1}{\mathcal{M}(\theta)} + O(\sigma^{-2}). \tag{5.15}$$

This represents a time-periodic asymptotic solution valid when $\sigma \gg 1$. Suppose that we compute a numerical solution to the governing equation (2.8) for a particular choice of parameter values and take $h_0(\theta)$ in the initial condition equation (2.10) to be a steady solution $h_s(\theta)$. Since $\Omega_T(T = 0) = 0$, we can fit equation (5.15) to the initial profile at $t = T = 0$ up to the second order in σ by setting $\kappa_1 = 0$. However, at second order there is no way to choose the constant κ_2 such that $h_2(T = 0) = 0$. We therefore have a discrepancy between the numerical solution and the asymptotic approximation of $O(\sigma^{-2})$. In figure 8, we demonstrate agreement between the numerical computation and the asymptotic solution equation (5.15) with $\kappa_1 = 0$. Here the numerical solution was obtained by integrating the characteristic system equation (4.1) forward in time from the starting profile $h_s(\theta)$, where $h_s(\theta)$ solves equation (3.2) with $\Omega = 1$ and $Q = 0.5$. The vertical axis shows the norm h_N defined to be the maximum value of $h - h_s(\theta + \sigma^{-1}\Omega_T)$ over $\theta \in [0, 2\pi)$ during the time integration period $t \in [0, 10/\sigma]$. A best fit curve $h_N = 0.1/\sigma^2$ is shown with a dashed red line.

The above discussion suggests that, for large σ at least, for a sufficiently carefully chosen initial condition it should be possible to obtain a time-periodic solution to equation (2.8) which does not overturn. However, overturning is expected for a general initial condition and we can use our theory to estimate the overturning time, t^*. In general the starting profile $h_0(\theta)$ in the initial condition equation (2.10) will not exactly meet the requirement that $F \equiv 0$, and so we expect transient growth in T according to equation (5.5). If we identify h_0 with h_s, where h_s solves equation (3.2) with $\Omega = 1$, it follows from equation (5.4) that $F = O(\sigma^{-2})$, and the asymptotic theory predicts transient growth so that the uniformity of the expansion equation (5.3) is destroyed when $t = O(\sigma^2)$. If instead we identify h_0 with a profile that does not solve equation (3.2) with $\Omega = 1$, then $F = O(1)$ and the expansion equation (5.3) fails when $t = O(1)$. We interpret the failure of the expansion as the signature of overturning. This viewpoint is supported by our numerical solutions to the full governing equation (2.8). For the overturning times reported in figure 7 we see that in panel (a), for which $F = O(1)$, t^* approaches a constant as $\sigma \to \infty$ in agreement with the preceding remarks. In panel (b), for which $F = O(\sigma^{-2})$, t^* grows apparently like σ^2. Evidently the onset of overturning can be considerably delayed in the high-frequency limit by a judicious choice of the initial condition.

(b) Low-frequency limit ($\sigma \ll 1$)

The numerical results shown in figure 4 suggest that when $\sigma \ll 1$ blow-up occurs when b exceeds a threshold value. This motivates an analysis in the low-frequency limit. As in the previous subsection, we follow a multiple scales approach, in this case with t as the fast time scale and $T = \sigma t$ as the slow time scale.

It is convenient at the outset to rescale the film thickness, writing $h(\theta, t, T) = \Omega^{1/2} H(\theta, t, T)$, where $\Omega(T) = 1 + b\cos T$. We assume $|b| < 1$ so that $\Omega > 0$ for all T. We then posit the expansion

$$H(\theta, t, T) = H_0(\theta, t, T) + \sigma H_1(\theta, t, T) + \sigma^2 H_2(\theta, t, T) + O(\sigma^3), \tag{5.16}$$

assuming $\sigma \ll 1$. Inserting into equation (5.2) we obtain at leading order, $O(1)$,

$$H_{0t} + \Omega(T)\left(H_0 - \frac{1}{3}H_0^3\cos\theta\right)_\theta = 0. \tag{5.17}$$

Following the discussion in §3, for a general initial condition we expect that H_0 will reach a slope singularity at a finite time t. However the solution will remain regular if at $t = 0$ the profile H_0 coincides with a t-independent solution of equation (5.17), that is, one that satisfies

$$H_0 - \frac{1}{3}H_0^3\cos\theta = q(T), \tag{5.18}$$

for some $q(T)$ to be determined later. We therefore insist that $H_0(\theta, T)$ solves equation (5.18). We note that this is essentially the same as the cubic equation (3.2) for the steady MP problem, with T playing the role of a parameter, and with the relationship $Q = \Omega^{3/2} q$. A question of interest, then, is whether $q(T)$ can reach the threshold value of $2/3$ identified in §3, and so drive the leading-order solution toward blow-up.

At first order, $O(\sigma)$,

$$H_{1t} + \Omega(M_0 H_1)_\theta = \Omega^{-1/2} R(\theta, T) \quad \text{and} \quad R_1 \equiv -(\Omega^{1/2} H_0)_T, \tag{5.19}$$

where $M_0(\theta, T) = 1 - H_0^2\cos\theta$. This essentially presents a forced version of the linear stability equation (3.10). The solution is

$$H_1 = \frac{1}{M_0}U_1(z) + \frac{1}{\Omega^{3/2}M_0}\int_\pi^\theta R_1(\xi)\,\mathrm{d}\xi, \tag{5.20}$$

where the function U_1 is arbitrary, $z = \Omega(T)t - \nu_0(\theta)$, and

$$\nu_0(\theta) \equiv \int_\pi^\theta \frac{\mathrm{d}\xi}{M_0(\xi)}. \tag{5.21}$$

We require H_1 to be 2π-periodic in θ. To check this we first differentiate equation (5.18) with respect to T, and rearrange to get

$$M_0 H_{0T} = q_T. \tag{5.22}$$

Integrating this with respect to θ,

$$\int_\pi^\theta H_{0T}\,\mathrm{d}\theta = \nu_0(\theta) q_T. \tag{5.23}$$

With reference to §3a we notice that $\nu_0(\theta)$ is composed of $a_0\theta$ plus a periodic function of θ. Rearranging equation (5.18), using the definition of M_0 and integrating with respect to θ, we

find

$$\int_\pi^\theta H_0\,\mathrm{d}\theta = 3\nu_0(\theta)q - 2\int_\pi^\theta \frac{H_0}{M_0}\,\mathrm{d}\theta. \tag{5.24}$$

Using equations (5.23) and equation (5.24) we may write

$$\int_\pi^\theta R_1(\xi)\,\mathrm{d}\xi = \Omega^{1/2}\nu_0(\theta)\left(q_T + \frac{3}{2}\frac{\Omega_T}{\Omega}q\right) - \frac{\Omega_T}{\Omega^{1/2}}\int_\pi^\theta \frac{H_0}{M_0}\,\mathrm{d}\xi. \tag{5.25}$$

If $q < 2/3$ then H_0 satisfying equation (5.18) is bounded and 2π-periodic in θ. The right-hand side of equation (5.25), and hence H_1, has the same properties if

$$q_T = \frac{\Omega_T}{\Omega}\left(\mathcal{H}(q) - \frac{3}{2}q\right), \tag{5.26}$$

where

$$\mathcal{H}(q) = \frac{1}{P_0}\int_0^{2\pi} \frac{H_0}{1 - H_0^2\cos\theta}\,\mathrm{d}\theta \quad \text{and} \quad P_0(q) = \int_0^{2\pi} \frac{1}{1 - H_0^2\cos\theta}\,\mathrm{d}\theta. \tag{5.27}$$

The solution for H_1 is then given by

$$H_1 = \frac{1}{M_0}U_1(z) - \frac{\Omega_T}{\Omega^{1/2}}\int_\pi^\theta \frac{H_0}{M_0}\,\mathrm{d}\xi. \tag{5.28}$$

It is clear from equation (5.28) that $H_{1\theta}$ is bounded. Furthermore, H_{1T} is bounded for all T provided that $|q_T| < \infty$ by virtue of equation (5.22).

The solution to the problem at $O(\sigma^n)$ has the form

$$H_n = \frac{1}{M_0}\left(U_n(z) + \int_\pi^\theta R_n(\xi)\,\mathrm{d}\xi\right), \tag{5.29}$$

with U_n arbitrary, and $R_n = -(\Omega^{1/2}H_{(n-1)})_T + (F_n\cos\theta)_\theta/3$, where the $F_n(H_0, H_1, \ldots, H_{n-1})$ are known (for example, $F_2 = 3H_0H_1^2$). Let us assume that the U_n are given for $n \geq 0$, for example by setting an appropriate initial condition at $t = T = 0$. Since, if $|q_T| < \infty$, H_n and $H_{n\theta}$ are both bounded for $n = 0$, 1, it is clear that the same property holds for $n \geq 2$. Given these remarks we expect the expansion equation (5.16) to remain uniform as time increases.

The nonlinear ordinary differential equation (5.26) determines $q(T)$. It has the invariant $\Omega^{1/2}\int_0^{2\pi} H_0\,\mathrm{d}\theta$, which means that fluid volume is conserved at leading order (this can be shown by differentiating equation (5.18) with respect to T and then by straightforward manipulations). Furthermore we can show that when $2/3 - q \ll 1$

$$\mathcal{H} \sim 1 + \frac{2 - (2/3 - q)^{1/2}}{2\log(2/3 - q)}. \tag{5.30}$$

Inserting this result into equation (5.26) we can then see that $q_T \to 0$ as $q \to 2/3$ and, moreover, $q_{TT} \to -\infty$ in the same limit. This behaviour is demonstrated numerically in figure 9a,b for $b = 0.5$ and initial condition $q(0) = 0.48$. Good agreement between the approximation equation (5.30), valid when $2/3 - q \ll 1$, and the numerically computed $\mathcal{H}(q)$, is shown in figure 9d.

When $q = 2/3$ the leading-order profile H_0 is described by the the heteroclinic connection along the separatrix that connects the saddle points at $\theta = 0$, 2π (see figure 1). In this case $\nu_0(\theta) \to \infty$ as $\theta \to 0$. A slight rearrangement of equation (5.25) is

$$\int_\pi^\theta R(\xi)\,\mathrm{d}\xi = \Omega^{1/2}\nu_0(\theta)\left(q_T + \frac{\Omega_T}{\Omega}\left[\frac{3}{2}q - 1\right]\right) + \frac{\Omega_T}{\Omega^{1/2}}\int_\pi^\theta \frac{(1 - H_0)}{M_0}\,\mathrm{d}\xi. \tag{5.31}$$

With the help of equation (5.18) written for $q = 2/3$ we can deduce that

$$\int_0^\pi \frac{(1 - H_0)}{M_0}\,\mathrm{d}\theta = \frac{1}{2}\int_0^\pi H_0\,\mathrm{d}\theta < \infty, \tag{5.32}$$

the inequality being clear given that the integral represents one half of the total fluid volume on the cylinder. Setting $q = 2/3$ in equation (5.31), and taking the limit $\theta \to 0$, we observe that the

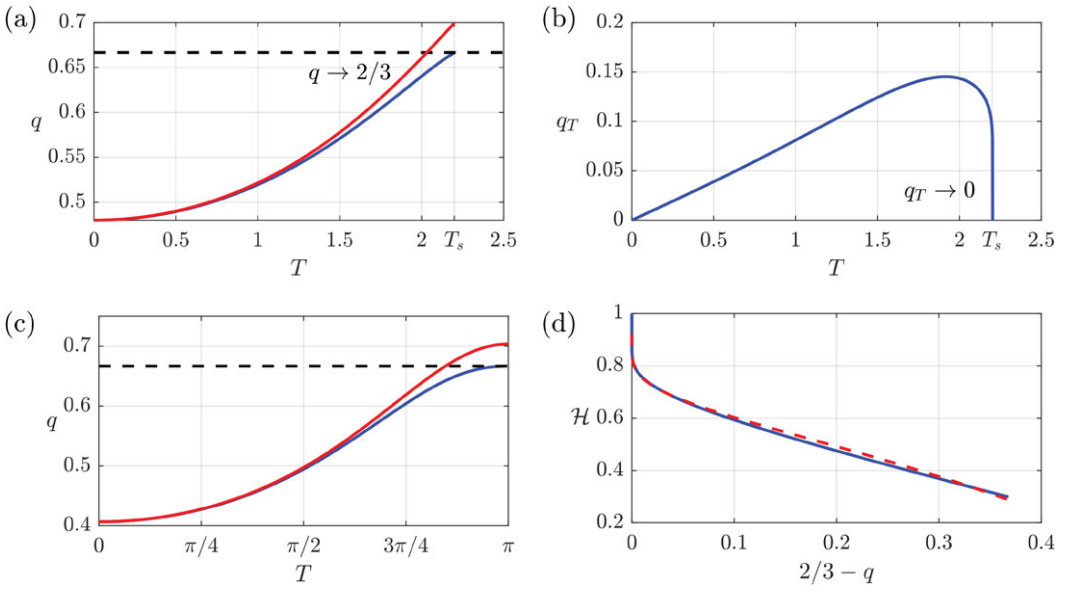

Figure 9. (a,b) Numerical solution of equation (5.26) (solid blue curves) for $q(0) = 0.48$ and $b = 0.5$. The integration is stopped at $T = T_s$ where $q(T_s) = 2/3$. In this case $T_s = 2.2$. The solid red curve shows the approximate $q(T)$ given in equation (5.35). (c) Numerical solution of equation (5.26) (solid blue curve) for $b = 0.5$ and $q(0) = q^*(0.5) \approx 0.4063$, with the approximate solution equation (5.35) shown with a red curve. (d) Comparison between $\mathcal{H}$ as defined in equation (5.27), shown with a blue solid line, and the approximation for $\mathcal{H}$ valid as $q \to 2/3$ given by equation (5.30), shown with a red dashed line.

terms in the large curved bracket on the right-hand side of equation (5.31) must vanish. Therefore in this case (cf. equation (5.26) for $q < 2/3$) we have

$$q_T = 0, \tag{5.33}$$

and it follows that $q = 2/3$ for all T. Unlike equation (5.26), this equation does not conserve the quantity $\Omega^{1/2} \int_0^{2\pi} H_0 \, \mathrm{d}\theta$ since in this case the integral has a fixed value and Ω varies with T.

Next we integrate equation (5.26) numerically starting from some $q(0)$. For $q(0) < q^*(b)$, where $q^*(b)$ is to be determined, q is periodic in time T. For $q(0) = q^*(b)$, we find that $q(\pi) = 2/3$ and $q_T(\pi) = 0$. If $q(0) > q^*(b)$ then $q(T_s) = 2/3$ with $q_T(T_s) > 0$ at some $T_s = T_s(q_0, b) > 0$. This heralds the breakdown of the approximation since a smooth solution of equation (5.18) ceases to exist (see the discussion in §3). Accordingly $q^*(b)$ describes a curve in the (b, q_0) plane which divides regular solutions of equation (5.26) from those which blow up. The implicit nonlinear relation for $q^*(b)$,

$$\int_{q^*}^{2/3} \frac{dq}{\mathcal{H}(q) - \frac{3}{2}q} = \log\left(\frac{1-b}{1+b}\right), \tag{5.34}$$

follows on integrating equation (5.26) from $T = 0$ to $T = \pi$. We solve this using Newton's method to obtain the $q^*(b)$ curve shown with a black solid line in figure 10.

As an alternative to integrating equation (5.26) numerically, a simple approximation to $q(T)$ can be found by first noting that the one-term Taylor expansion about $q = 0$, given by $\mathcal{H} \approx q$, holds good unless q is very close to 2/3 (this is confirmed by comparison with the numerical solution to equation (5.34)). With this approximation equation (5.26) simplifies to $q_T = -(\Omega_T/2\Omega)q$, which can be integrated exactly to yield

$$q(T) = q_0 \frac{\Omega_0^{1/2}}{\Omega^{1/2}}, \tag{5.35}$$

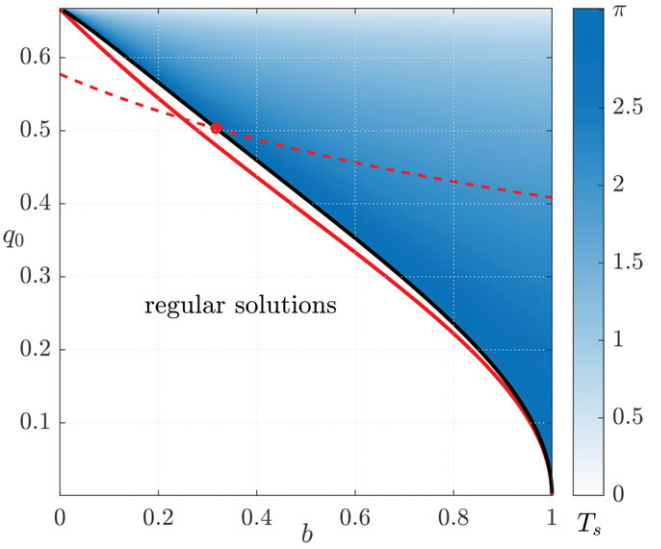

Figure 10. Regularity map for $q(T)$ solving equation (5.26) in the limit $\sigma \to 0$. The black curve delineates the boundary $q^*(b)$ between regular behaviour ($q(T)$ periodic in T) and blow-up behaviour ($q(T) \to 2/3$ as $T \to T_s$). The red curve shows the approximation to the $q^*(b)$ boundary given in equation (5.36). The dashed red line shows $1/q_0 = \sqrt{3(1+b)}$, whose intersection with the black line at $b = 0.317$, shown with a red marker point, determines the location of the red marker point in figure 4.

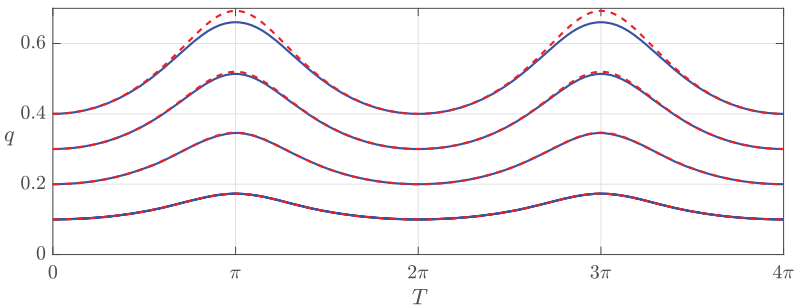

Figure 11. Numerical integration (blue curves) of equation (5.26) for $b = 0.5$ and and $q(0) = 0.1, 0.2, 0.3, 0.4$ (bottom to top). The dashed red lines show the approximation equation (5.35). In this case $q^*(0.5) = 0.4063$.

where $q_0 = q(0)$ and $\Omega_0 = \Omega(0) = 1 + b$. This result immediately provides the approximation to the $q^*(b)$ curve shown with a solid red line in figure 10,

$$q^*(b) = \frac{2}{3}\left(\frac{1-b}{1+b}\right)^{1/2}. \tag{5.36}$$

In figure 11 we compare the approximation equation (5.35) with the solution of the full equation (5.26) for the case $b = 0.5$ and for a number of different initial conditions, $q(0)$. Evidently the approximation performs very well with the greatest discrepancy occurring at the maxima for the larger values of $q(0)$.

It is instructive to compare the present small-σ asymptotic results with numerical solutions to the full governing equation (2.8). First, we note that for $q_0 < q^*(b)$ the dependence of the solution on both t and T indicates that the small-σ solution will in general be quasiperiodic, and this is consistent with the comment made earlier in §4 (see also figure 5). Figure 12 shows time snapshots of the surface profiles obtained by integrating the full governing equation (2.8) numerically for a

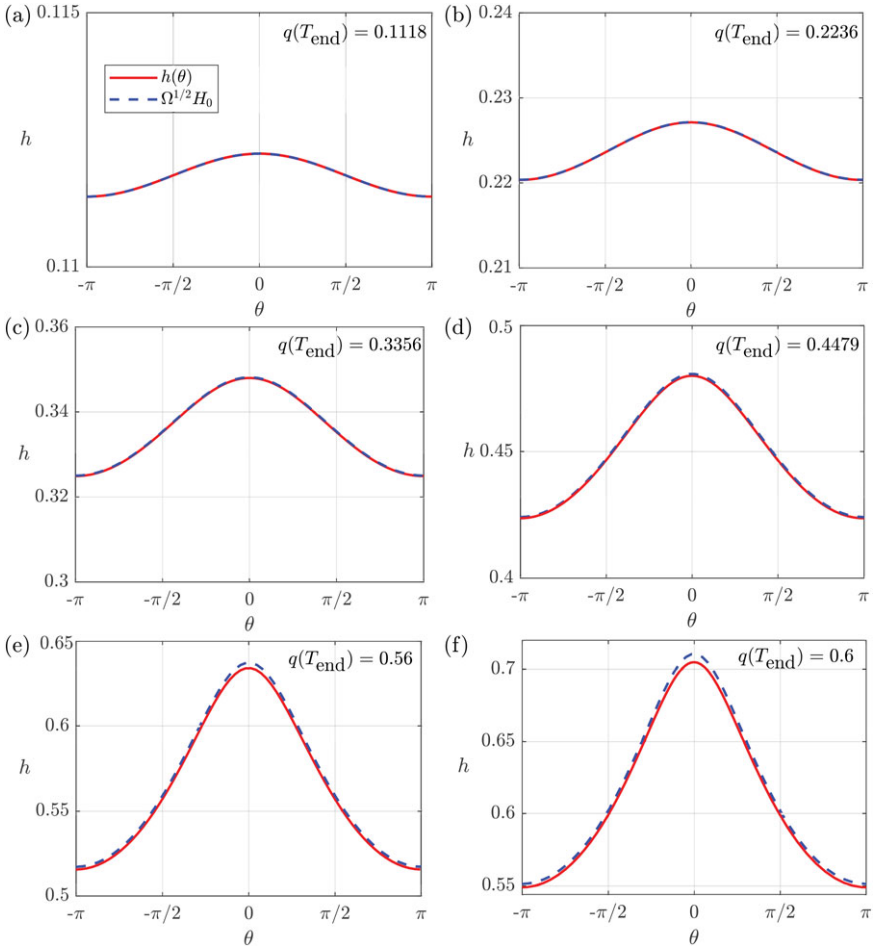

Figure 12. Film profiles (solid red curves) obtained by integrating equation (2.8) numerically up to $t_{\text{end}} = T_{\text{end}}/\sigma = 2000/\sigma$ for the case $b = 0.25$ and $\sigma = 0.01$. The initial condition is equation (2.10) with $h_0 \in \mathcal{H}$ and $\mathcal{Q}_0 = q_0\Omega_0^{3/2}$ where $\Omega_0 = \Omega(0) = 1 + b$ and (a) $q_0 = 0.1$, (b) $q_0 = 0.2$, (c) $q_0 = 0.3$, (d) $q_0 = 0.4$, (e) $q_0 = 0.5$, and (f) $q_0 = 0.5385$. For panel (f) q_0 is very close to the critical value $q^*(0.25) \approx 0.538725$. The dashed blue lines show $\Omega^{1/2}H_0$, where H_0 is the leading-order solution in the small-σ analysis of §5b, satisfying equation (5.18) with $q(0) = q_0$ and using the approximate solution equation (5.35) for $q(T)$.

variety of initial conditions equation (2.10) with $h_0 \in \mathcal{H}$. The leading-order asymptotic solution, using the approximation equation (5.35) for $q(T)$, is included for comparison. The agreement between the two sets of results is generally excellent, but with some discrepancy at the surface maximum seen when q gets close to 2/3.

In figure 7a, we show the numerically computed overturning time t^* for the case $b = 0.5$ and $q_0 = 0.5$. These parameter values correspond to a point in the white regular region in figure 10. We can match the expansion equation (5.16) to the initial condition used in figure 7a by taking $H_0(\theta, 0, 0) = h_0$, and $H_n(\theta, 0, 0) = 0$ for $n \geq 1$ (the latter can be effected by choosing the arbitrary functions U_n in equation (5.29) appropriately). Accordingly the asymptotics predict no overturning in the limit $\sigma \to 0$ and this is in line with the very rapid growth of t^* observed in figure 7a in this limit. In contrast figure 7b shows the overturning time for the same value of b but with the initial profile solving $h_0 - (1/3)h_0^3 \cos\theta = 1/2$. Matching the asymptotic expansion equation (5.16) to this initial condition, at leading order we find that equation (5.18) is not satisfied at $T = 0$ and, consequently, the solution of the leading-order equation (5.17) will develop a slope

singularity at a finite time, as was discussed in §3. The predicted overturning time $t^* = 242$ obtained by integrating equation (5.17) with Ω fixed at its initial value $\Omega(0) = 1 + b$, is shown with a dashed line in figure 7b.

The blow-up that occurs at $T_s = T_s(q_0, b)$ in the blue region in figure 10 (i.e. for $q^*(b) < q_0 < 2/3$) can be interpreted as the overturning of the film profile in the full problem. At $T = T_s$ we expect the expansion equation (5.16) to disorder, yielding the approximation to the overturning time for the full problem $t^* = T_s(q_0, b)\sigma^{-1}$ valid for $\sigma \ll 1$. In figure 7c we showed the overturning time for the case $b = 0.5$, $q_0 = \sqrt{2}/3 = 0.471$ corresponding to a point in the blow-up region in figure 10. With this value of q_0, integrating equation (5.26) we compute $T_s = 2.270$ and hence the prediction $t^* = 2.270\sigma^{-1}$. This is shown with a red dashed line in figure 7c. At sufficiently small σ it is in excellent agreement with the numerically computed overturning time for the full governing equation.

Finally, we note that the present results are consistent with the blow-up map shown earlier in figure 4. For this figure, trajectories solving equation (4.1) were computed with the initial condition equation (4.3) and $h^* = 1/\sqrt{3}$. This means that, in the context of the present small σ analysis, the relevant trajectories start on the (θ, H_0) curve with $q_0 = 1/\sqrt{3(1+b)}$. This curve is shown with a red dashed line in figure 10, and where it intersects the black curve representing $q^*(b)$ gives the threshold b value for small-σ blow-up in figure 4. The intersection is found to occur at $b = 0.317$. This is shown with a red marker in figure 4, where it can be seen to be in good agreement with the boundary curve between regular and blow-up behaviour at small σ.

(i) Single shock solution for $q = 2/3$

Under the small-σ assumption, according to equation (5.33) if $q(0) = 2/3$ then $q = 2/3$ for all T. If we take the surface profile for $q = 2/3$ to be H_0 satisfying equation (5.18) and given by the solid gold separatrix curve in figure 2, a contradiction arises since conservation of mass at leading order requires $\Omega^{1/2}\int_0^{2\pi} H_0\,\mathrm{d}\theta$ and Ω is T-dependent. We can circumvent the mass conservation issue by following Johnson [19] to introduce a shock at a location $\theta^{\mathrm{s}}(T) > 0$. The film profile follows the solid separatrix curve in figure 2 over $-\pi \le \theta \le \theta^{\mathrm{s}}$ (proceeding smoothly through the saddle at $\theta = 0$ onto the dashed part of the separatrix curve where $H_0 > 1$) and then, at $\theta = \theta^{\mathrm{s}}$, it drops vertically down to the solid part of the separatrix below and continues along this up to $\theta = \pi$.

A shock solution allows the cylinder to support a larger liquid volume than a smooth solution. The liquid volume increases monotonically as θ_s varies from 0 for which $V^*/2\pi \approx 0.70708140$, up to $\theta_s = \pi/2$ for which value the film has infinite thickness at the shock, but the finite volume

$$V_{\max} = 6\Omega^{1/2}\sum_{n=1}^{3}\int_{a_n}^{b_n}\frac{\mathrm{d}H}{(H+2)^{1/2}(H^3+3H-2)^{1/2}}, \tag{5.37}$$

where $(a_1, b_1) = (H_m, 1)$, $(a_2, b_2) = (1, \infty)$, $(a_3, b_3) = (H_m, 2/3)$. Here H_m is the minimum of H on the separatrix which occurs at $\theta = \pm\pi$. We calculate $V_{\max}/(2\pi\,\Omega^{1/2}) \approx 1.102317$, which agrees with the value quoted by Villegas-Diaz *et al.* [28].

Suppose that we start at $T = 0$ with a leading-order profile H_0 featuring a shock located at $\theta = \theta^s(0)$ with $0 < \theta^s(0) \le \pi/2$. The fluid volume $V(T) = \int_0^{2\pi} H_0\,\mathrm{d}\theta$. As time increases the shock location $\theta^s(T)$ must adjust to ensure mass conservation, i.e. such that $\Omega^{1/2}V(T) = (1+b)^{1/2}V(0)$. The requirement that $|\theta^{\mathrm{s}}| < \pi/2$ imposes the constraint

$$\left(\frac{1+b}{1-b}\right)^{1/2}\frac{V(0)}{V_{\max}} \le 1. \tag{5.38}$$

This places an upper limit on the modulation amplitude, b, for a given initial volume.

(ii) Double shock solution for $q < 2/3$

Up to this point the discussion for $q(T) < 2/3$ has assumed that the leading-order term H_0 is such that $\Omega^{1/2}H_0 \in \mathcal{H}$ at $t = T = 0$ with H_0 a smooth function (i.e. no shocks). Johnson [19] demonstrated that one can construct double-shock solutions for which the film profile exhibits

a bulge in fluid thickness enclosed by the two shocks. Referring to the phase portrait in figure 2, we see that a double-shock solution can be put together by following one of the blue trajectories at the bottom of the figure for a chosen Q, and then, somewhere in the interval $-\pi/2 < \theta < \pi/2$, jumping up to and then back down from the equivalent Q curve at the top of the figure, and then continuing along the original trajectory to complete the profile. It is not necessary that the jumps be located symmetrically about $\theta = 0$.

A case of particular interest is that of zero flux, $Q = 0$, indicated by the broken blue line in figure 2. For $Q = 0$, and in the absence of shocks, the only static solution is a film of zero thickness. For the double-shock solution a solitary mass of fluid with compact support is carried around by the cylinder, with the fluid inside recirculating (Johnson [19] describes how to extend the thin-film model to include next order terms and allow for a boundary layer around each shock to facilitate this recirculation). The maximum scaled volume that can be supported in this case can be expressed by

$$\frac{V^0_{\max}}{2\pi} = \frac{\sqrt{3}}{\pi}\int_0^{\pi/2} \frac{\mathrm{d}\theta}{\sqrt{\cos\theta}} = \frac{2\sqrt{3}}{\pi} F\left(\frac{\pi}{4};\sqrt{2}\right) \approx 1.44562, \tag{5.39}$$

where F is the incomplete elliptic integral of the first kind (e.g. Olver *et al.* [31]).

Assume for our small-σ problem that a double shock is present in the leading-order profile H_0. Let the jumps be located at $\theta = \theta_L < 0$ and $\theta_R > 0$ with $|\theta_{L,R}| \leq \pi/2$. Since $\Omega^{1/2}\int_0^{2\pi} H_0\,\mathrm{d}\theta$ is automatically conserved as q evolves according to equation (5.26), the shock locations $\theta_{L,R}$ do not depend on T and so remain fixed. If $q(0) < q^*(b)$ then $q(T)$ is T-periodic and will oscillate in the range $(0, 2/3)$ with the double shock profile adjusting accordingly. If $q(0) \geq q^*(b)$ then $q(T) \to 2/3$ as $T \to T_1$, for some finite T_1, with $q_T(T_1) > 0$; in this case, we jump to the single shock solution described in the previous subsection.

6. Conclusion

We have examined the dynamics of a thin viscous liquid film flowing on the outside of a horizontal cylinder which is rotating about its axis with an angular velocity that includes a steady part and a time-periodic part. Surface tension has been neglected. If the time-periodic component of the angular velocity is removed, the problem reduces to that studied by Moffatt [1] and Pukhnachev [4], and subsequent authors.

Our review of the constant rotation rate MP problem included a novel perspective on describing steady solutions using a phase-plane analysis. This perspective makes plain visually the steady solution space, including both smooth solutions and those exhibiting shocks. It also makes clear graphically the threshold on the rotation rate for a steady solution to exist, and the onset of dripping that is expected if this threshold is exceeded. A separatrix in the relevant phase portrait delineates a boundary representing the extreme continuous steady solution which supports the maximum fluid volume (although larger volumes are possible for solutions with shocks).

The introduction of a time-periodic part into the angular velocity fundamentally alters the behaviour of the system. Naïvely one might expect that if the Moffatt criterion is violated during part of the cycle (i.e. if the surface profile goes above the gold solid line in figure 2), then blow-up will occur. This intuition holds good in the low-frequency limit, where it is effectively the Moffatt threshold that dictates matters: single-valued quasiperiodic solutions occur beneath this threshold, and blow-up occurs when it is exceeded. But in general the situation is not so simple for the Moffatt criterion can be temporarily violated yet the flow recovers without blow-up. For the case of steady rotation, an infinite slope singularity is reached at a finite time unless the initial condition is chosen to coincide with a steady solution (which exists provided the Moffatt criterion is satisfied). Similarly, for time-periodic rotation, in general the dynamics progress toward an infinite slope singularity and the formation of a shock. It is an interesting question as to whether one can choose an initial condition to avoid this and maintain a regular, single-valued solution. We made some progress toward answering this in the high-frequency and low-frequency limits, as we shall review below.

On tracking a single point on the film surface by solving the characteristic equations for the governing partial differential equation, we found that, for some values of the forcing amplitude and frequency, the point remains bounded, meaning that its normal distance from the cylinder remains finite. However, for forcing amplitude and frequency values lying in a certain set, the point diverges from the cylinder surface, pointing to the blow-up of the film. However, such an interpretation should be made with caution since the divergence occurs after the formation of a slope singularity, and the loss of single-valuedness, of the full film profile. Nevertheless, the dynamics of the characteristic system is interesting *per se*, and using numerical computations we mapped out the divergent set in detail, revealing its highly intricate, and seemingly fractal, structure, with sharp protrusions around the base frequency (and rational multiples thereof) of the corresponding unforced oscillator.

To develop a deeper understanding of the dynamics we also performed asymptotic analyses in the limits of high and low forcing frequency. In the former case a multiple-scales analysis suggested that the flow is time-periodic if the initial condition is chosen sufficiently carefully. For a general initial condition the film profile will overturn; but this overturning can be considerably delayed by choosing the initial condition to coincide with a Moffatt–Puchnachev steady profile. A multiple-scales approach was also used in the low-frequency limit. In this case we derived a secularity condition which reveals a threshold modulation amplitude beyond which a singularity is reached at some time. This singularity, which heralds the breakdown of the multiple-scales expansion, was interpreted as indicating the blow-up of the solution to the full problem, and confirmation of this point was provided through comparison with numerical solutions of the full problem. Regular, bounded solutions exist below the threshold amplitude, and it was shown that these correspond to quasiperiodic solutions of the full problem. Single and double shock solutions for which the film jumps instantaneously in height, were also discussed. In both cases the abrupt change in height can be smoothed by introducing boundary layers as discussed by Johnson [19].

In summary, our results have revealed a complex interplay between the amplitude and frequency of the torsional movement of the cylinder and the stability and regularity of the liquid film. We have focused on a non-zero mean forcing, but the case of zero-mean forcing, for example $\Omega(t) = b\cos\sigma t$, is also interesting. In this case the low-frequency equation (5.26) remains valid, with $\Omega(T) = b\cos T$, up to $T = \pi/2$. The approximate solution equation (5.35) suggests that $q \to 2/3$ for any pair (q_0, b), so that blow-up always occurs and no quasiperiodic, low-frequency solution can be constructed. We leave further investigation of this case to a future study. As in Moffatt's original work we have herein neglected the effect of surface tension. The influence of this force on the dynamics of the film in the presence of a modulated rotation rate is the subject of our ongoing research.

Data accessibility. This article has no additional data.

Declaration of AI use. We have not used AI-assisted technologies in creating this article.

Authors' contributions. A.J.B.-L.: writing—original draft; M.G.B.: writing—original draft.

Both authors gave final approval for publication and agreed to be held accountable for the work performed therein.

Conflict of interest declaration. We declare we have no competing interests.

Funding. This work was partially supported by the research project, PID2023-151343NB-C32 financed by MICIU/AEI/10.13039/501100011033/FEDER, UE. A.J.B.-L. would like to thank the Spanish Ministry of Science, Innovation and Universities for the financial support provided by the Fellowship PRE2021-099112 that allowed his research stay in the School of Mathematics at the University of East Anglia.

Appendix A

We demonstrate that $M = \Omega - h_s^2\cos\theta$ is positive for all $\theta \in [0, 2\pi)$, where $h_s(\theta)$ satisfies

$$\Omega h_s - \frac{1}{3}h_s^3\cos\theta = Q, \tag{A 1}$$

for constant Ω, provided that $Q < (2/3)\Omega^{3/2}$. Writing $h_s = \Omega^{1/2}H$, $Q = \Omega^{3/2}q$, and manipulating equation (A 1), we have

$$M = \frac{2\Omega}{H}\left(\frac{3}{2}q - H\right), \tag{A 2}$$

where $q < 2/3$. The case $\cos\theta = 0$ is clear since then $H = q$. Assuming $\cos\theta > 0$ and writing $H = (\cos\theta)^{-1/2}R$, equation (A 1) becomes

$$g(R) = \lambda, \tag{A 3}$$

where $\lambda = (\cos\theta)^{1/2}q < 2/3$ and $g(x) \equiv x - x^3/3$. The cubic equation (A 3) has three real roots, and it is clear that the root of interest is that for which $0 < R < 1$ (refer to figure 2; the other positive root has $R > 1$ and will produce blow-up). Evidently $g(x) > 2x/3$ for $0 < x < 1$ since over this range $g(x) - 2x/3 = x(1 - x^2)/3 > 0$. It follows that $\lambda > 2R/3$ and, consequently, $H < 3q/2$ so that $M > 0$. A similar, but slightly simpler, argument applies in the case when $\cos\theta < 0$.

References

1. Moffatt HK. 1977 Behaviour of a viscous film on the outer surface of a rotating cylinder. *J. Mécanique* **16**, 651–673.
2. Ribatski G, Jacobi AM. 2005 Falling-film evaporation on horizontal tubes—a critical review. *Int. J. Refrig.* **28**, 635–653. (doi:10.1016/j.ijrefrig.2004.12.002)
3. Herczyński A, Cernuschi C, Mahadevan L. 2011 Painting with drops, jets, and sheets. *Phys. Today* **64**, 31–36. (doi:10.1063/1.3603916)
4. Pukhnachev VV. 1977 Motion of a liquid film on the surface of a rotating cylinder in a gravitational field. *J. Appl. Mech. Tech. Phys.* **18**, 344–351. (doi:10.1007/BF00851656)
5. Hinch EJ, Kelmanson MA. 2003 On the decay and drift of free-surface perturbations in viscous thin-film flow exterior to a rotating cylinder. *Proc. R. Soc. Lond. A* **459**, 1193–1213. (doi:10.1098/rspa.2002.1069)
6. Hinch EJ, Kelmanson MA, Metcalfe PD. 2004 Shock-like free-surface perturbations in low-surface-tension, viscous, thin-film flow exterior to a rotating cylinder. *Proc. R. Soc. Lond. A* **460**, 2975–2991. (doi:10.1098/rspa.2004.1327)
7. Hansen EB, Kelmanson MA. 1994 Steady, viscous, free-surface flow on a rotating cylinder. *J. Fluid Mech.* **272**, 91–108. (doi:10.1017/S0022112094004398)
8. Peterson RC, Jimack PK, Kelmanson MA. 2001 On the stability of viscous free-surface flow supported by a rotating cylinder. *Proc. R. Soc. Lond. A* **457**, 1427–1445. (doi:10.1098/rspa.2000.0780)
9. Duffy BR, Wilson SK. 1999 Thin-film and curtain flows on the outside of a rotating horizontal cylinder. *J. Fluid Mech.* **394**, 29–49. (doi:10.1017/S0022112099005558)
10. Evans PL, Schwartz LW, Roy RV. 2004 Steady and unsteady solutions for coating flow on a rotating horizontal cylinder: two-dimensional theoretical and numerical modeling. *Phys. Fluids* **16**, 2742–2756. (doi:10.1063/1.1758943)
11. Evans PL, Schwartz LW, Roy RV. 2005 Three-dimensional solutions for coating flow on a rotating horizontal cylinder: theory and experiment. *Phys. Fluids* **17**, 072102. (doi:10.1063/1.1942523)
12. Noakes CJ, King JR, Riley DS. 2005 On three-dimensional stability of a uniform, rigidly rotating film on a rotating cylinder. *Q. J. Mech. Appl. Math.* **58**, 229–256. (doi:10.1093/qjmamj/hbi011)
13. Lopes AB, Thiele U, Hazel AL. 2018 On the multiple solutions of coating and rimming flows on rotating cylinders. *J. Fluid Mech.* **835**, 540–574. (doi:10.1017/jfm.2017.756)
14. Kelmanson MA. 2009 On inertial effects in the Moffatt–Pukhnachov coating-flow problem. *J. Fluid Mech.* **633**, 327–353. (doi:10.1017/S0022112009006703)
15. Noakes CJ, King JR, Riley DS. 2006 On the development of rational approximations incorporating inertial effects in coating and rimming flows: a multiple-scales approach. *Q. J. Mech. Appl. Math.* **59**, 163–190. (doi:10.1093/qjmam/hbj001)
16. Wray AW, Cimpeanu R. 2020 Reduced-order modelling of thick inertial ows around rotating cylinders. *J. Fluid Mech.* **898**, A1–1. (doi:10.1017/jfm.2020.421)
17. Karabut EA. 2007 Two regimes of liquid film flow on a rotating cylinder. *J. Appl. Mech. Tech. Phys.* **48**, 55–64. (doi:0021-8944/07/4801-0055)

18. Gorla RSR. 2000 Rupture of thin power-law liquid film on a cylinder. *J. Appl. Mech.* **68**, 294–297. (doi:10.1115/1.1355033)
19. Johnson R. 1988 Steady-state coating flows inside a rotating horizontal cylinder. *J. Fluid Mech.* **190**, 321–342. (doi:10.1017/S0022112088001338)
20. Badali D, Chugunova M, Pelinovsky DE, Pollack S. 2011 Regularized shock solutions in coating flows with small surface tension. *Phys. Fluids* **23**, 093103. (doi:10.1063/1.3635535)
21. Benilov E, Benilov MS, O'Brien S. 2009 Existence and stability of regularized shock solutions, with applications to rimming flows. *J. Eng. Math.* **63**, 197–212. (doi:10.1007/s10665-008-9227-1)
22. O'Brien S. 2002 Linear stability of rimming flow. *Q. Appl. Math.* **60**, 201–211. (doi:10.1090/qam/1900490)
23. Villegas-Díaz M, Power H, Riley DS. 2003 On the stability of rimming flows to two-dimensional disturbances. *Fluid Dyn. Res.* **33**, 141–172. (doi:10.1016/S0169-5983(03)00043-1)
24. Lopes AVB. 2018 *Dynamics of Free Surface Flows on Rotating Cylinders*. UK: The University of Manchester.
25. O'Brien S, Gath E. 1998 The location of a shock in rimming flow. *Phys. Fluids* **10**, 1040–1042. (doi:10.1063/1.869630)
26. Benilov ES, O'Brien SBG. 2005 Inertial instability of a liquid film inside a rotating horizontal cylinder. *Phys. Fluids* **17**, 052106. (doi:10.1063/1.1905964)
27. Benilov ES, Lapin VN. 2013 Inertial instability of flows on the inside or outside of a rotating horizontal cylinder. *J. Fluid Mech.* **736**, 107–129. (doi:10.1017/jfm.2013.530)
28. Villegas-Díaz M, Power H, Riley DS. 2005 Analytical and numerical studies of the stability of thin-film rimming flow subject to surface shear. *J. Fluid Mech.* **541**, 317–344. (doi:10.1017/S0022112005006142)
29. Benilov E, O'Brien S, Sazonov I. 2003 A new type of instability: explosive disturbances in a liquid film inside a rotating horizontal cylinder. *J. Fluid Mech.* **497**, 201–224. (doi:10.1017/S0022112003006633)
30. Guckenheimer J, Holmes P. 2002 *Nonlinear oscillations, dynamical systems, and bifurcations of vector fields*, 7th edn. Applied Mathematical Sciences, vol. 42. New York, USA: Springer.
31. Olver FW, Lozier DW, Boisvert RF, Clark CW. 2010 *NIST handbook of mathematical functions*. New York, USA: Cambridge University Press.